LEEWARD CENTERLINE AND SIDE FUSELAGE ENTRY HEATING PREDICTIONS FOR THE SPACE SHUTTLE ORBITER

Vernon T. Helms III
NASA Langley Research Center
Hampton, Virginia

SUMMARY

Heat transfer data measured along the leeward centerline and on the side fuselage of the Space Shuttle orbiter during STS-2 and STS-3 are compared with predictions of empirical heating techniques derived from wind-tunnel tests. Steps required to extrapolate an existing leeward centerline theory to flight conditions are described. Generally favorable comparisons from Mach 24 down to approximately Mach 7 for both flights are presented. The side fuselage impingement heating method is currently under development, but some preliminary results are available. The method is briefly described and compared with wind-tunnel and flight measurements. Side heating predictions are given for an STS-3 trajectory point near Mach 10 showing good agreement with flight data. There is evidence of embedded vortices emanating from the side fuselage impingement line which significantly enhance local heating rates at both wind-tunnel and flight conditions.

INTRODUCTION

Heating on top of the Space Shuttle orbiter's vortex-dominated fuselage is a complex function of Mach number, Reynolds number, and angle of attack. The upper fuselage thermal environment is generally characterized in terms of heating to the leeward centerline where heating rates can be relatively high.[1-3] An empirical technique for predicting top centerline heating on the orbiter has been developed and successfully applied to wind-tunnel data covering a large range in Reynolds number and angle of attack at Mach 6 and 10.[4] This method consists of a modified turbulent swept cylinder correlation using an effective local sweep angle that is measured directly from oil-flow patterns on the upper fuselage. A consistent relationship was demonstrated between the axial distribution of measured sweep angles and the distribution of top centerline heating. This report explains how to extrapolate these wind-tunnel sweep angles to account for conditions at flight Reynolds numbers and Mach numbers. Comparisons of leeward centerline heating predictions with flight values are then presented.

The basic concepts for a new technique designed to predict heating along the side fuselage impingement line are also presented here. This method uses the same form of heating equation as the top centerline theory. Furthermore, it makes use of similar assumptions concerning the relationship between surface flow directions and the side fuselage impingement heating distribution. The side fuselage method is derived from oil-flow and phase-change paint wind-tunnel data and supplemented by thermocouple measurements. Although the side impingement method is still under development, some promising preliminary comparisons have been made with both wind-tunnel and flight heating rates.

SYMBOLS

AFFDL	Air Force Flight Development Laboratory
C	Chapman-Rubesin coefficient
L	characteristic length of wind-tunnel model or full-scale vehicle as indicated
M	Mach number
OMS	Orbital Maneuvering System
q_c	convective heating rate
q_{c_h}	stagnation heating rate on a sphere with radius equal to average height of orbiter flat side body
q_{c_o}	stagnation heating rate on a scaled one-foot radius sphere in the free stream
q_{c_s}	stagnation heating rate on a sphere with radius equal to that of orbiter top fuselage
Re	Reynolds number, based on L unless otherwise specified
s	cross-sectional surface running length measured from top centerline
STS	Space Transportation System
T	temperature
x	axial length measured from orbiter's nose
℄	centerline
α	angle of attack
α_r	reference α defined in equation (5)
β	bow shock angle measured with respect to free stream direction
δ	flow deflection angle across bow shock
ε	surface flow angle and local angle of attack
η	change in sweep angle with respect to angle of attack
η'	change in η with respect to x/L

Λ	effective sweep angle
Λ_r	reference Λ defined in quations (3), (4), and (5)
ν	Prandtl-Meyer turning angle
ϕ	Mach number correction factor
$\bar{\chi}$	hypersonic viscous-interaction parameter = $M^3\sqrt{C}/\sqrt{Re}$ (see reference 5)

Subscripts

D	in equation (1), twice the orbiter upper fuselage radius; in equation (16), twice the average height of orbiter flat side body
ext	extrapolated
f	flight condition
L	quantity based on characteristic length
ℓ	quantity based on local flow properties
max	maximum value
t	wind-tunnel condition
∞	free stream

WIND-TUNNEL DATA

Oil flow patterns used to extrapolate the leeward centerline heating method to flight conditions were obtained on the upper fuselage of a 0.01-scale orbiter model in air in the Langley Research Center's Mach 6 and Mach 10 facilities,[6-8] and also on a 0.006-scale model in 20-Inch Mach 14 AFFDL wind tunnel at Wright-Patterson Air Force Base.[9] Tests at Mach 6 ranged from 15° to 40° angle of attack at Reynolds numbers of 2.7×10^6, 5.4×10^6, and 7.3×10^6. Oil flows at Mach 10 were run at α = 15° to 45° for free-stream Reynolds numbers of 0.59×10^6, 1.19×10^6, and 2.37×10^6. Angles of attack of 15° to 40° at $Re_\infty = 0.280 \times 10^6$ and 0.423×10^6 were used at Mach 14.

The phase-change paint heat transfer, oil flow, and thermocouple measurements used to derive the side fuselage impingement heating method were made on 0.01-scale Shuttle orbiter models in Langley's Mach 6 and Mach 10 tunnels. Tests were conducted for $Re_\infty = 0.59 - 7.3 \times 10^6$ and at angles of attack of 20°, 30°, and 40°. Oil-flow tests were made using an aluminum model. Models for the phase-change paint heating measurements were constructed of a filled epoxy casting compound and a semi-infinite slab solution[10] was assumed during data reduction. The supplemental thermocouple results were drawn from a previously unpublished data base described in reference 4.

FLIGHT DATA

Flight measurements used for comparison with the top centerline and side fuselage heating methods were obtained on STS-2 and STS-3 at the locations shown in figure 1. The top centerline heating rates, measured by calorimeters, were the only data from STS-2 that were used in this report. The convective component of heat transfer for the calorimeters was determined by adding the radiative loss term to the calorimeter value. Heating due to solar radiation was then subtracted for those trajectory points where the instruments were in sunlight. The effect of solar heating was computed by the technique of reference 11. All of the instrument locations for STS-3 were occupied by thermocouples. A one-dimensional, transient-conduction analysis[12] was used to determine convective heating for these instruments with solar radiation heating, once again, computed separately.* A process combining the results of trajectory and atmospheric reconstruction provided information on vehicle attitude and free stream conditions.[13,14]

LEEWARD CENTERLINE HEATING

Review of Theory

The empirical leeward centerline heating method described in reference 4 is embodied in the equation

$$q_c = 0.75\, q_{c_s}\, Re_{\ell,D}^{0.3}\, (0.002975 + 0.003423 \cos\Lambda) \tag{1}$$

The parameter q_{c_s} is the stagnation heating rate on a sphere with a radius equal to that of the Shuttle's upper fuselage. The Reynolds number is based on twice that radius. Both quantities are defined by local leeside flow properties computed using the flow model shown in figure 2. It was determined that the bow shock angle, β, through which free stream flow is processed must be equal to 2α. The flow deflection angle, δ, depends on M_∞ and β. The Prandtl-Meyer angle, ν, required to expand the flow to the Shuttle's upper fuselage is the sum of δ and α.

A pivitol feature of the theory is the close relationship between axial variations in heating and changes in upper fuselage surface flow directions, Λ, measured from oil flow photographs. The technique used to measure oil-flow patterns is illustrated in figure 3. The angle, ε, between the top centerline and a line drawn tangent to the oil-flow path inflection point is

*Heating rates reduced from STS-3 thermocouple data and solar-heating corrections for STS-2 and STS-3 were provided by D. A. Throckmorton, Aerothermodynamics Branch, Space Systems Division, Langley Research Center.

equated with the local angle of attack of flow approaching the top fuselage. The local sweep angle is thus defined as

$$\Lambda = 90° - \varepsilon \tag{2}$$

Figure 4 shows two sets of wind-tunnel data where the measured sweep angles and the corresponding values of normalized heating rate are plotted as a function of x/L at two different test conditions. It is readily apparent that sweep angle and top centerline heating vary in an inverse fashion. A more appropriate term for Λ is "effective" sweep angle because, as defined for the purpose of the top centerline method, its value often becomes larger than 90°. Effective sweep angles greater than 90° are generally associated with inboard flow in the vicinity of the leeward centerline or with surface patterns caused by flow circulation ahead of the OMS pods and vertical tail. This is simply a mathematical convenience which allows the theory to penetrate zones on the leeward meridian where heating is influenced by various classes of separated flow patterns.[4] Using this approach, it was demonstrated that the leeward centerline theory is able to cope with the diverse heating environments represented by the wind-tunnel data. As an example, figure 5 shows a comparison of the theory's heating predictions with wind-tunnel data at the two test conditions indicated in figure 4.

Extrapolation to Flight Conditions

The wind-tunnel data base of upper fuselage surface flow directions is presented in figures 6, 7, and 8 where axial distributions of measured sweep angles for Mach numbers of 6, 10, and 14, respectively, are plotted for each angle of attack and Reynolds number combination. The hypersonic viscous-interaction parameter is also given for each test condition since this term is often used to classify the general behavior of leeside separated flow. Sweep angles from x/L = 0.383 to 0.731 correspond to axial locations where thermocouples were positioned on the wind-tunnel model. Additional measurements from x/L = 0.30 to 0.787 were made to encompass the locations of orbiter flight instrumentation. For a given Mach number, the Reynolds numbers in flight are considerably higher than those in the wind tunnel. Conversely, flight Mach numbers are greater than in the wind-tunnel data for corresponding Reynolds numbers. The ground-to-flight difference in each of these parameters will affect both upper-surface flow patterns and leeward centerline heating. Details of the many complex flow interactions which determine upper fuselage heating and surface flow patterns cannot be directly addressed due to the lack of information concerning the specific nature of leeside flow processes. However, it will be demonstrated that the relatively simple approach described here for extrapolating the leeward centerline heating equation and wind-tunnel sweep angles to flight conditions is able to capture the essential trends of the Reynolds number and Mach number influences on top centerline heating.

The first step toward converting the empirical leeward centerline heating method into a flight prediction technique is to establish a procedure for extrapolating the wind-tunnel sweep angles to their equivalent flight Reynolds number values. The next step is to define a criterion which relates the flight environment at each trajectory point to the proper set of wind-tunnel test conditions in order to duplicate flight trends in leeward centerline heating distributions. A third requirement is to develop a method of correcting for the effects of the differential between flight Mach numbers and the wind-tunnel Mach number from which the flight sweep angle distribution is to be extrapolated. The solution to these three problems will now be investigated.

A Reynolds number correction for the upper fuselage surface flow patterns may be obtained through manipulation of the sweep-angle data base. The data for each Mach number were cross-plotted in a variety of ways in order to reveal the format which optimized the effect of Reynolds number related trends. No easily discernable or consistent Reynolds number trends could be found in the Mach 6 data, which correspond to low values of $\overline{\chi}_\infty$. The mixed trends in the data for figure 6 also suggest that a majority of the Mach 6 sweep angle distributions are relatively independent of Reynolds number. It was concluded that the sweep angles measured over the Reynolds number range indicated in figure 6 require no overall correction for the effect of flight Reynolds number. However, flow angles for the different Mach 6 tests must still be linked to the appropriate range of flight conditions in a manner that is yet to be described. Similarly, sweep angles for the two free stream conditions near Mach 14, where $\overline{\chi}_\infty$ is large, were found to be nearly identical for most test cases. Only the surface flow directions at Mach 10, for intermediate values of $\overline{\chi}_\infty$, were subject to significant variations as a function of Reynolds number. Rough estimates for the range of $\overline{\chi}_\infty$ where wind-tunnel data must be corrected for the effects of flight Reynolds numbers can be offered on the basis of these assessments. The lower bound of this range may be $\overline{\chi}_\infty \approx 0.2$ to 0.3. These numbers are close to the maximum value for the Mach 6 tests but well below the lowest Mach 10 parameter for which, as will be discussed below, there is a strong Reynolds number effect. The upper bound on the range of $\overline{\chi}_\infty$, where Reynolds number corrections are required, is perhaps 1.5 or less. This is based on the observation that the axial sweep angle distribution for $\alpha = 45°$ at $M_\infty = 10.16$ and $\overline{\chi}_\infty = 1.219$ in figure 7 is similar to those at Mach 14 for lower angles of attack in figure 8. These Mach 10 flow patterns are still dependent on Re_∞, but it is suggested that a moderate increase in $\overline{\chi}_\infty$ may dissolve the association with Reynolds number.

The Mach 10 data exhibited very clear Reynolds number relationships by plotting sweep angles at all Reynolds numbers versus angle of attack for each axial location. This is illustrated for $x/L = 0.51$ in figure 9. Linear curve fits are used to indicate general trends of the flow-angle measurements at each of the three Reynolds numbers. Individual data points usually fall within $\pm 10°$ of the corresponding curve fit. An increase in Reynolds number increases the rate of change of the sweep angle as a function of angle of attack. The linear curve fits for each Reynolds number share one common value of sweep angle and angle of attack, denoted by Λ_r and α_r, where local flow directions are independent of Reynolds number. Plots like the one in figure 9 for other axial locations reveal variations in Λ_r and α_r that depend on x/L. The axial dependence of Λ_r is shown in figure 10. In a broad sense, Λ_r is an indication of the average magnitude of sweep angles on the upper fuselage at each axial station. The large values of Λ_r for $0.2 < x/L < 0.34$ are due to the influence of the canopy and the initiation of the leeside vortex flow patterns. The effect of the canopy diminishes with increasing axial length and leeside flow becomes well established beyond $x/L = 0.34$. As a result, Λ_r is nearly constant until reaching $x/L = 0.63$ where it begins to rise again. This is due to the forward extent of surface patterns with reversed flow directions, particularly at large angles of attack and high Reynolds numbers, caused by flow interactions with the blunt forward face of the OMS pods and with the vertical tail. The straight-line segments in figure 10 which approximate Λ_r are defined as follows:

$$\text{for } 0.2 < x/L < 0.34 \quad \Lambda_r = 117.7° - 133.7° (x/L) \tag{3}$$

$$\text{for } 0.34 \leq x/L \leq 0.63 \quad \Lambda_r = 72.0° \tag{4}$$

$$\text{for } 0.63 < x/L < 0.8 \quad \Lambda_r = 1.3° + 112.3° (x/L) \tag{5}$$

Figure 11 shows that α_r varies linearly and decreases with increasing x/L. This is primarily caused by the flow interactions at aft axial stations mentioned above. Effective sweep angles within the resulting surface flow patterns are elevated at high values of α and Re_∞. This forces the point of intersection for the various Reynolds number distributions, like those in figure 9, to lower angles of attack. The linear curve fit for α_r is given by

$$\alpha_r = 40.1° - 29.5° (x/L) \tag{6}$$

The parameters Λ_r and α_r will be used as part of the procedure to correct Mach 10 wind-tunnel sweep angles for the effects of flight Reynolds numbers.

A basic property of the Reynolds number correction for local flow directions is related to the slopes of the linear distributions of Λ vs α. A well-defined Reynolds number relationship develops when the slopes of the linear curve fits for each Reynolds number, $\eta = \Delta\Lambda/\Delta\alpha$, are plotted against x/L as in figure 12. The slope of Λ vs α, η, becomes larger at all axial stations with increasing Reynolds number. Each Reynolds number produces a maximum value of η at $x/L = 0.445$ as also shown by the straight-line curve fits for the data. The rate of change of η with respect to x/L depends on axial location and Reynolds number. This is shown in figure 13 where $\eta' = \Delta\eta/\Delta(x/L)$ is presented as a function of log Re_∞ for locations both fore and aft of $x/L = 0.445$. These terms are defined as follows:

$$\text{for } x/L < 0.445 \quad \eta' = -11.059 + 2.542 \log Re_\infty \tag{7}$$

$$\text{for } x/L > 0.445 \quad \eta' = 15.429 - 3.297 \log Re_\infty \tag{8}$$

The variation of η at $x/L = 0.445$ provides the information which allows extrapolation of the entire Mach 10 sweep angle data base to higher Reynolds numbers corresponding to flight conditions. Figure 14 indicates that the three wind-tunnel data points that are available form a linear function of log Re_∞ which is given as

$$\eta_{max} = -13.332 + 2.424 \log Re_\infty \tag{9}$$

The dispersion of each data point from the linear correlation is quite small. This would appear to confine the error band of the extrapolation to a very narrow range up to Reynolds numbers at least an order of magnitude larger than the wind-tunnel values.

The assessment of Reynolds number effects on sweep angles for the various sets of wind-tunnel data and the extrapolation of the Mach 10 upper fuselage flow patterns to their equivalent flight Reynolds number form described above complete the first step required of applying the empirical leeward-centerline heating method to flight conditions. The second step, which was outlined earlier, involves the definition of a criterion that relates flight conditions to the proper set of wind-tunnel test data. The purpose of this is to insure that general trends in heating predictions will reproduce the axial distributions of flight heating measurements. The most direct way of obtaining this information is to collect heating distributions at various entry trajectory points and observe which of the wind-tunnel tests produce a corresponding inverse variation in sweep angles. Examples of such comparisons are illustrated in figures 15 through 17 for Mach numbers from 24 to approximately 7. Both flights produced nearly the same leeward centerline heating distributions at corresponding trajectory points. However, heating rates measured by calorimeters on STS-2 are higher than the thermocouple-derived heat-transfer rates for STS-3 at similar flight conditions. This point will be discussed later. In each case it is noted that the correct distribution of sweep angles corresponds to a wind-tunnel test for which the free stream Reynolds number is roughly 40 percent of the flight Reynolds number. A study of orbiter leeside heating in reference 15 also found that trends in ground-based heating rates appeared during entry only at flight Reynolds numbers that were considerably higher than in the wind tunnel. Apparently, the wind-tunnel environment more accurately simulates flight flow structures on the upper fuselage at higher Reynolds numbers over a wide Mach number range. For practical purposes, it is sufficient to use the set of wind-tunnel sweep angles for a freestream Reynolds number that is closest to 40 percent of the flight value. This allows nearly complete coverage of the orbiter's entry trajectory instead of having heating predictions at only a few discrete flight conditions. This relationship seems to be independent of either wind-tunnel or flight Mach number, which indicates that the distribution of leeward centerline heating is almost exclusively a function of free stream Reynolds number. According to this criterion, top centerline heating predictions at early entry times for STS-2 and STS-3 should use wind-tunnel sweep angles from the Mach 14 data. Flight heating distributions from $M_\infty = 20$ down to around 10 require the extrapolated Mach 10 Λ's. Trajectory points below this will use the Mach 6 wind-tunnel data.

Heating rates on STS-2 using calorimeters were significantly above the STS-3 thermocouple heating measurements. A general dissatisfaction with the calorimeters' performance on STS-1 and STS-2 resulted in their removal. There is also the unsettled question concerning hot-to-cold wall effects on heating rates measured by calorimeters. It can be expected that the large temperature differential which existed between the relatively cool calorimeters and the surrounding hot surface areas would cause these instruments to register a higher heating rate than was actually present. The thermocouple data do not suffer from this problem. For these reasons, the determination of a Mach number effect on leeward centerline flight heating predictions was based on thermocouple measurements from flight 3.

Heating predictions based on the Reynolds number extrapolation of wind-tunnel sweep angles will be required to obtain the Mach number correction. The following is a step-by-step set of instructions on how to use the Reynolds number correction. Heating predictions for a given trajectory point will make use of sweep angles at the wind-tunnel Reynolds number closest to 40 percent of the flight Reynolds number

$$Re_{\infty,t} = 0.4\ Re_{\infty,f} \tag{10}$$

Calculate η_{max} and η' for both Reynolds numbers. Next determine η at the desired axial location using the expressions

$$\eta_f = \eta_{max,f} - (0.445 - x/L)\eta'_f \tag{11a}$$

$$\eta_t = \eta_{max,t} - (0.445 - x/L)\eta'_t \tag{11b}$$

Now compute Λ for each Reynolds number at the desired angle of attack assuming a linear curve fit of Λ vs α, as in figure 9, using the relationships

$$\Lambda_f = \Lambda_r + (\alpha - \alpha_r)\eta_f \tag{12a}$$

$$\Lambda_t = \Lambda_r + (\alpha - \alpha_r)\eta_t \tag{12b}$$

The change in sweep angle required to extrapolate the ground-based Λ to the flight Reynolds number is the difference between Λ_f and Λ_t, thus

$$\Lambda_{ext} = \Lambda + (\Lambda_f - \Lambda_t) \tag{13}$$

where Λ is interpolated for x/L and α from the wind-tunnel data set identified by equation (10). Usually, $\Lambda \neq \Lambda_t$ because the linear distribution containing Λ_t is only meant to be a general representation of the measurements. However, the difference between two such linear representations for a given x/L and α is a direct measure of the effect of changing the Reynolds number. These steps must be repeated for all axial locations where heating predictions are to be made.

The lack of wind-tunnel data at very high Mach numbers precludes the possibility of extracting a Mach number effect on upper fuselage flow directions, and the associated leeward centerline heating, from the available ground tests. As with the criterion relating flight-heating distributions to wind-tunnel surface flow patterns, the effect of flight Mach number on the extrapolated heating prediction must be formulated using a small portion of the entry data. Heating rates at $M_\infty = 14.0$, $Re_\infty = 3.52 \times 10^6$, and $\alpha = 40.9°$ for flight three were chosen at random and plotted in figure 18(a) along with three sets of heating predictions calculated using the MINIVER[5] aerodynamic heating computer program. The highest heating predictions resulted from applying the uncorrected wind-tunnel sweep angles for $M_\infty = 10.34$ and $Re_\infty = 1.19 \times 10^6$ directly to the flight environment. The set of predictions at intermediate heating levels shows the effect of using the Reynolds number extrapolation outlined in equations (10) through (13). The result of this procedure is a predicted heating distribution that displays the general trends of the flight measurements, but the predictions are higher by almost a factor of two. This residual is assumed to be related to the difference between the flight and wind-tunnel Mach numbers. It can be accounted for at the Mach 14 trajectory point by multiplying heating rates for the Reynolds number extrapolation by a Mach number correction factor, ϕ, given as

$$\phi = (M_{\infty,t}/M_{\infty,f})^2 \tag{14}$$

The modified Reynolds-number corrected predictions are in good agreement with the measured heating rates. This factor was proven to yield results that were consistent with flight data at other trajectory points, as shown in figure 18(b) for $M_\infty = 20.0$, $Re_\infty = 1.53 \times 10^6$, and $\alpha = 39.8°$. The corresponding wind-tunnel sweep angles were for $M_\infty = 10.16$ and $Re_\infty = 0.59 \times 10^6$. Three sets of predictions are plotted as before. There is a much larger effect of Mach number at this entry point. But the Mach number correction in equation (14) places the fully corrected predictions very close to the flight data. Figure 18 demonstrates that the wind tunnel to flight difference in both Mach number and Reynolds number is important for predicting the magnitude of flight heat transfer to the orbiter's leeward meridian. By incorporating the Reynolds number extrapolation, the criterion for reproducing the flight heating distribution and the Mach number correction, equation (1) can now be written as

$$q_c = 0.75 q_{c_s} \phi \, Re_{\ell,D}^{0.3} (0.002975 + 0.003428 \cos \Lambda_{ext}) \tag{15}$$

At flight conditions requiring the use of wind-tunnel sweep angles from the Mach 6 or Mach 14 tests, Λ_{ext} is assumed to be equal to Λ.

Comparison of Leeward Centerline Heating Predictions With Flight Data

Figures 19 and 20 present comparisons of leeward centerline heating predictions with entry measurements made at Mach numbers from 24 to 7 during STS-2 and STS-3, respectively. Similar free stream conditions for each trajectory are shown here so that measurements and theory for both flights may be compared. Calorimeter measurements of heating rate on STS-2 are consistently above the thermocouple data of flight 3 by 50 percent to 100 percent or more. The largest differences occur at free stream Mach numbers greater than 20 and less than 10. Heating predictions for the two flights at approximately the same free stream conditions and angle of attack are at about the same level. This indicates that the discrepancy in heating measurements may be due to instrumental effects rather than large variations in the flight environment. The magnitude of predicted heating tends to agree more closely with STS-3 thermocouple measurements. The predicted axial distribution of heating rate is much the same as flight measurements of heating distributions for both entry trajectories. The very large disagreement between theory and flight data below Mach 10 on STS-2 may be another symptom of instrumental effects, as might be the case for $M_\infty > 20$. The comparisons at low Mach numbers for STS-3 are much closer.

Evidence for transition from laminar to turbulent flow can be seen in these comparisons, particularly in the thermocouple data of flight 3. Most of the predicted heating rates, which are turbulent, are higher than measured values by a factor of approximately two for $M_\infty > 20$. This is a clear indication of laminar flow on the upper fuselage at very high Mach numbers.

The theory and flight data rapidly converge for both flights beginning near $M_\infty = 20$. The entire leeward centerline appears to become turbulent within a very short time. However, another study[15] of leeward centerline heating for STS-3 concludes that transition to turbulent flow occurs no earlier than $M_\infty \approx 18$. This difference may be related to the corrections applied to wind-tunnel sweep angles used for heating predictions in the vicinity of $M_\infty = 20$. It was noted earlier that the high angle of attack, low Reynolds number Mach 10 flow patterns bear a resemblance to the Mach 14 sweep angles for which no Reynolds number correction is required. Perhaps by virtue of their relatively large value of $\overline{\chi}_\infty$, the low Reynolds number Mach 10 flow angles used in the $M_\infty = 20$ heating prediction may require less correction for Reynolds number effects than was imposed by the wind-tunnel extrapolation. If so, predicted heating rates could be higher than those indicated for the Mach 20 STS-3 trajectory point. This would shift the realm of fully turbulent flow to somewhat lower Mach numbers. But if such an influence of the viscous interaction parameter exists, it is not readily apparent in the available wind tunnel data. Even though corrections for this kind of second order effect may be necessary for heating predictions to agree exactly with flight data, the first-order corrections presented here produce favorable comparisons with entry heating measurements.

SIDE FUSELAGE HEATING

Basic Concepts of Theory

An empirical method for predicting side fuselage impingement heating on the Shuttle orbiter is under development. It is based on an analysis of oil-flow patterns and corresponding phase-change paint and thermocouple heating measurements. The side fuselage theory uses the same form of turbulent heating equation as for the wind-tunnel top centerline correlation. The equation as derived for $M_\infty = 10.36$, $Re_\infty = 2.37 \times 10^6$, and $\alpha = 40°$, since these parameters are close to the conditions for which flight comparisons will be made, is

$$q_c = 0.42\, q_{c_h}\, Re_{\ell,D}^{0.3}\, (0.003531 + 0.004069 \cos \Lambda) \tag{16}$$

The factor 0.42 corrects the reference heating rate, q_{c_h}, from the stagnation value on a sphere to that on a sharp-cornered slab of infinite length with a half width equal to the average height of the side fuselage flat surface. Reynolds number and the reference heating rate are based on local flow parameters that are computed using the methods outlined below, and the coefficients are determined by iteration using only a few data points at different values of Re_∞.

The surface oil-flow directions radiating away from the impingement line are also taken to represent angle of attack of flow approaching the side fuselage and, thus, a sweep angle in the same sense as illustrated in figure 3 for the upper body. The axial variation of sweep angle along the impingement location is shown in figure 21 for $M_\infty = 10$ and $\alpha = 40°$. Sweep angles on the side fuselage show little change with Reynolds number. They are constant over the forward portion of the impingement line and increase sharply at large values of x/L. The increase in Λ was determined to be a result of an additional expansion of the flow before reaching the fuselage. Both factors contribute to a rapid fall in impingement heating at those locations.

The source of the impinging flow is assumed to be the shear layer which originates along a separation line on the strake's upper surface. It is further assumed that separation-point shear-layer flow properties are proportional to those at the same axial location on the strake's leading edge. Variations in leading-edge flow properties along the strake were accounted for by interpolation of pressure distributions computed by the three-dimensional High Alpha Inviscid Solution (HALIS)[17] computer code.* It was found that pressure increases linearly along the extent of the strake. Another simplifying assumption states that leading edge flow from a given fractional distance along the strake will influence heating at the same fractional distance along the side fuselage impingement line. This model allows the flow to travel downstream as it moves upward and over toward the fuselage.

These procedures were incorporated into the MINIVER computer program. Figure 22 shows an example of a comparison between the theory's side fuselage impingement line heating predictions and phase-change paint measurements for the test condition of $M_\infty = 10.36$, $Re_\infty = 2.37 \times 10^6$, and $\alpha = 40°$. The initial rise in heating is due to the increase in pressure along the strake's leading edge combined with the constant Λ's in figure 21. Peak heating occurs just forward of $x/L = 0.4$ corresponding to the location at which sweep angles begin to increase. Larger sweep angles and the additional expansion of flow beyond this point cause a rapid reduction of impingement heating. The heating predictions are in close agreement with wind-tunnel data over the entire length of the impingement line. Similar comparisons have been obtained for all test conditions at Mach 10 which includes angles of attack from 20° to 40° and free stream Reynolds numbers of 0.59×10^6, 1.19×10^6, and 2.37×10^6.

Comparisons With Flight Data

The effect of Mach number on the heating prediction has not yet been assessed. Therefore, a preliminary comparison with flight data has been limited to the STS-3 trajectory point where $M_\infty = 10.37$, $Re_\infty = 5.41 \times 10^6$, and $\alpha = 38.9°$. Flight Mach number and angle of attack are within the range of the wind-tunnel conditions. The flight Reynolds number is larger by over a factor of two. But wind-tunnel sweep angles, as well as the impingement location, showed little change with Reynolds number at a given angle of attack. Values of Λ and impingement location for $\alpha = 38.9°$ were interpolated from the wind-tunnel measurements and applied to the flight prediction. Figure 23 shows the resulting axial distribution of impingement heating rate for the

*Existing HALIS flow-field computations were supplied by K. James Weilmuenster, Aerothermodynamics Branch, Space Systems Division, Langley Research Center.

selected flight parameters. The peak heating rate is approximately ten times higher than the average top centerline heating at this same trajectory point.

It is difficult for the relatively few instruments on the orbiter's side fuselage to obtain a direct measurement of impingement heating. Figure 24 shows the predicted location of flow impingement in relation to the positions of the side fuselage thermocouples. However, a comparison of the heating prediction shown in figure 23 with flight data can be accomplished as illustrated in figure 25. Cross-sectional measurements of heating at six axial stations are presented along with the predicted impingement heating for each value of x/L. Wind-tunnel measurements indicate that flow impingement moves off of the upper side fuselage near $x/L = 0.65$ for $\alpha \approx 40°$, so only data for $x/L \leq 0.594$ are used here. The next downstream array of orbiter instruments is at $x/L = 0.696$. The heating distributions superimposed on the data points were taken from wind-tunnel phase-change paint measurements for $M_\infty = 10.36$, $Re_\infty = 2.37 \times 10^6$ at $\alpha = 40°$ and normalized by the predicted impingement heating. The flight heating data generally conform to the trend and magnitude of the projected distributions. This seems to indicate that the impingement heating prediction is near the correct level.

Flight data at $x/L = 0.497$ and $x/L = 0.542$ contain some heating measurements that are approximately 80 and 120 percent above the mean local values, respectively. Figure 26 shows that these pulses of high convective heating are associated with large and erratic excursions in surface temperature which occur at later entry times. Similar temperature fluctuations affect many of the side fuselage thermocouple locations at slightly different times, but these variations are always confined to the high Reynolds number portion of the trajectory. The anomaly at $x/L = 0.497$ is above the impingement line while at $x/L = 0.594$ it is well below the impingement location. Many similar heating "spikes" were observed in the wind-tunnel data for Mach 6 and Mach 10, but only at locations above the impingement line. This is illustrated in figure 27 using one of the Mach 6 test cases for which Reynolds number is the same as for the STS-3 trajectory point. The average increase over local heating associated with these features in the wind tunnel was about 70 percent. The phase-change paint data revealed that the phenomena are highly localized, as indicated by the slender heating profile in figure 27. This same profile was applied to the data in figure 25 using dashed lines in order to distinguish actual flight measurements from normalized wind-tunnel heating.

It is suggested that these elevated local heating rates are caused by embedded vortices which are generated by viscous interactions during the impingement process. Embedded vortices are believed to be caused by boundary-layer cross-flow instabilities.[18] References 19 and 20 are two examples of the many studies on the relation between embedded streamwise vorticity and flow impingement. Figure 28 contains a photograph showing a sequence of uniformly spaced streaks in phase change paint above, and originating from, the impingement location on the orbiter model's side fuselage at a Mach 6 test condition. Each streak is thought to represent a very thin line of vortex impingement which produces locally higher heating, and the magnitude of heating decreases along its length. Side fuselage "streak" heating has also been noted on an early phase B orbiter configuration[21] and on the ASSET entry vehicle.[22] A larger number of streaks were observed in the phase-change paint tests with increasing Reynolds number and higher angles of attack. Streaks were present for all test conditions except $\alpha = 20°$ and 30° for Mach 10.

These trends indicate that side fuselage "streak" heating may well be expected to occur in the entry flight regime containing the selected STS-3 trajectory point. In addition, the changing number of streaks and variations in the spacing between them at different free-stream conditions and angles of attack mean that embedded vortices on the orbiter in flight will move longitudinally on the side fuselage. This motion will cause a number of individual vortices to sweep across a fixed location resulting in intermittent locally higher heating. This could explain the large temperature variations at later entry times shown in figure 26. Very large side fuselage STS-2 heating rates that have been previously documented[23] may also be caused by the onset of embedded vorticity.

CONCLUDING REMARKS

A method has been developed for extrapolating a wind-tunnel-developed empirical heating technique for the Space Shuttle orbiter's leeward centerline to flight conditions. The distribution of heating along the vehicle's leeward meridian was found to be primarily a function of Reynolds number. Axial heating trends in flight correspond to those in the wind tunnel for which the Reynolds number is approximately 40 percent of the flight value. Only those wind-tunnel leeside fuselage flow patterns at intermediate values of $\overline{\chi}_\infty$ displayed significant and consistent sensitivity to changes in Reynolds number. The effect of Mach number on heating predictions was determined through limited use of the flight data. Application of the extrapolated heating method to the flight environments of STS-2 and STS-3 produced generally favorable comparisons. It was tentatively concluded that the STS-2 heating measurements were of lower quality than those of STS-3. The theory may provide a somewhat conservative indication for the time of transition from laminar to turbulent flow. Heating predictions afforded by this procedure are adequate for the design of upper fuselage thermal protection systems.

A new technique for computing side fuselage impingement heating was briefly described. This method is derived from the leeward centerline theory. Although still under development, the side fuselage heating method was shown to agree well with wind-tunnel data and with selected STS-3 flight measurements. The comparison with flight data revealed that, as in the wind tunnel, there are areas of locally enhanced heating at side fuselage locations well away from the impingement line. The associated heating rates were approximately 100 percent higher than nearby undisturbed levels. It is suggested that this phenomenon is caused by embedded vortices resulting from viscous interactions that are perhaps related to flow reattachment at free-stream conditions which satisfy critical values of Mach number and Reynolds number at a given angle of attack. The existence of these features will have an impact on thermal protection requirements of future winged entry vehicles which experience flow impingement on the side fuselage.

REFERENCES

1. Whitehead, A. H., Jr., Hefner, J. N., and Rao, D. M., "Lee Surface Vortex Effects Over Configurations in Hypersonic Flow." AIAA Paper No. 72-77, January 1972.

2. Hefner, J. N., "Lee-Surface Heating and Flow Phenomena on Space Shuttle Orbiters at Large Angles of Attack and Hypersonic Speeds." NASA TN D-7088, 1972.

3. Zakkay, V., Miyazawa, M., and Wang, C. R., "Hypersonic Lee Surface Flow Phenomena Over Space Shuttle at Large Angles of Attack at $M_\infty = 6$." NASA CR-132501, 1974.

4. Helms, Vernon T., III, "An Empirical Method for Computing Leeside Centerline Heating on the Space Shuttle Orbiter." AIAA Paper No. 81-1043, June 1981.

5. Bertram, Mitchel H., "Hypersonic Laminar Viscous-Interaction Effects On the Aerodynamics of Two-Dimensional Wedge and Triangular Planform Wings," NASA TN D-3523, August 1966.

6. Goldberg, Theodore J., and Hefner, Jerry N. (Appendix by Emery, James C.), "Starting Phenomena for Hypersonic Inlets With Thick Turbulent Boundary Layers at Mach 6." NASA TN D-6280, 1971.

7. Schaefer, William T., Jr., "Characteristics of Major Active Wind Tunnels at the Langley Research Center." NASA TM X-1130, 1965.

8. Dunavant, James C., and Stone, Howard W., "Effect of Roughness on Heat Transfer to Hemisphere Cylinders at Mach Numbers of 10.4 and 11.4." NASA TN D-3871, 1967.

9. Gregorek, G. M., and Lee, J. D., "Design, Performance and Operational Characteristics of the ARL 20-Inch Hypersonic Wind Tunnel." Report No. ARL 62-392, Aeronautical Research Labs, Wright Patterson Air Force Base, August 1962.

10. Jones, Robert A., and Hunt, James L. "Use of Fusible Temperature Indicators for Obtaining Quantitative Aerodynamic Heat-Transfer Data." NASA TR R-230, February 1966.

11. Throckmorton, D. A., "Influence of Radiant Energy Exchange on the Determination of Convective Heat Transfer Rates to Orbiter Leeside Surfaces During Entry." AIAA Paper No. 82-0824, June 1982.

12. Throckmorton, D. A., "Benchmark Aerodynamic Heat Transfer Data from the First Flight of the Space Shuttle Orbiter." AIAA Paper No. 82-0003, January 1982.

13. Compton, H. R., Findlay. J. T., Kelly, G. M., and Heck, M. L., "Shuttle (STS-1) Entry Trajectory Reconstruction." AIAA Paper No. 81-2459, November 1981.

14. Price, J. M., "Atmospheric Definition for Shuttle Aerothermodynamic Investigations." Journal of Spacecraft and Rockets, Vol. 20, March-April 1983, pp. 133-140.

15. Throckmorton, D. A., and Zoby, E. V., "Orbiter Entry Leeside Heat Transfer Data Analysis." AIAA Paper No. 83-0484, January 1983.

16. Hender, D. R., "A Miniature Version of the JA70 Aerodynamic Heating Computer Program, H800 (MINIVER)." McDonnell Douglas Astronautics Company, MDC G0462, June 1970, Revised January 1972.

17. Weilmuenster, K. James, and Hamilton, H. Harris, II, "A Method for Computation of Inviscid Three-Dimensional Flow Over Blunt Bodies Having Large Embedded Subsonic Regions." AIAA Paper No. 81-1203, 1981.

18. Morkovin, Mark V., "Observations on Streamwise Vortices in Laminar and Turbulent Boundary Layers." NASA CR-159061, April 1979.

19. Seegmiller, H. L., "Surface-Flow Visualization Investigation of a Delta Wing Shuttle Configuration at a Mach Number of 7.4 and Several Reynolds Numbers." NASA TM X-62036, June 1970.

20. Ginoux, J. J., "On Some Properties of Reattaching Laminar and Transitional High Speed Flows." Von Karman Institute, Belgium, Technical Note 53, September 1969.

21. Matthews, R. L., Buchanan, T. D., Martindale, W. R., and Warmbrod, J. D., "Experimental and Theoretical Aerodynamic Heating and Flow Field Analysis of a Space Shuttle Orbiter." NASA TM X-2507, pp. 261-296, February 1972.

22. Pagel, L. L., Beardsley, P. P., and Gaumer, G. R., "ASSET Volume IV Correlative Analysis of Heat Transfer Data." AFFDL-TR-65-31, Volume IX, April 1966.

23. Lee, D. B., and Harthun, M. H., "Aerothermodynamic Entry Environment of the Space Shuttle Orbiter." AIAA Paper No. 82-0821, June 1982.

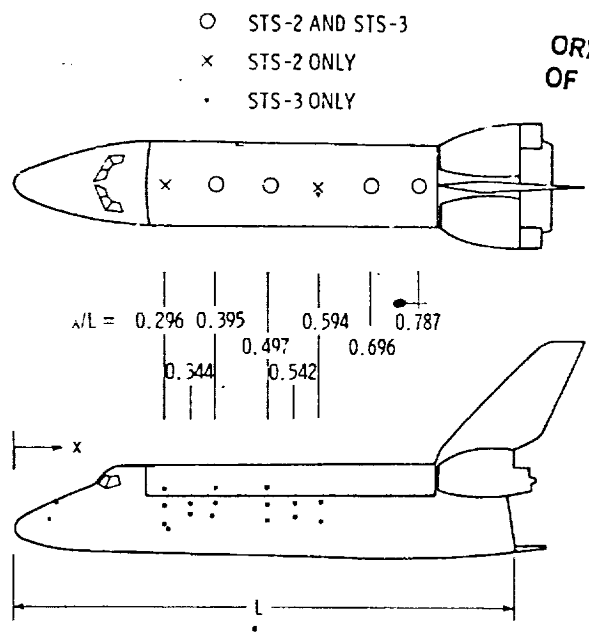

Figure 1.- Locations of entry heating rate measurements on Shuttle orbiter's fuselage.

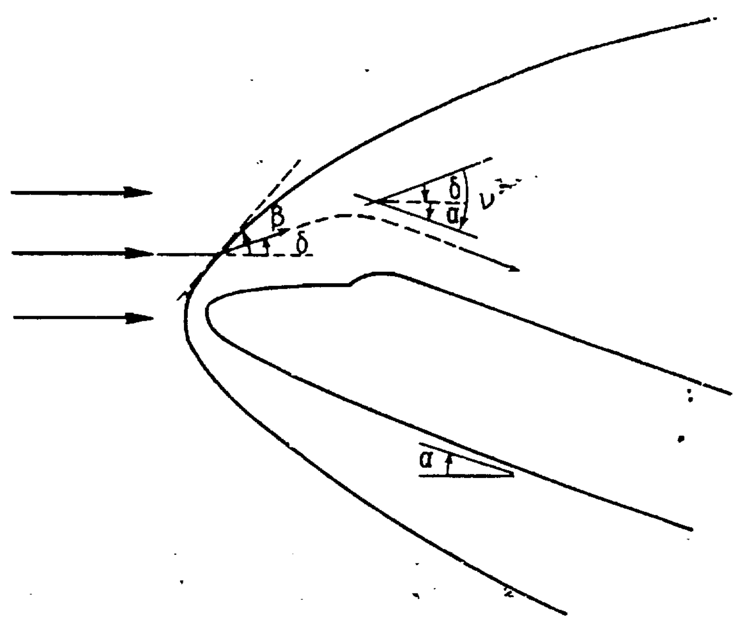

Figure 2.- Flow field model used to compute local leeside properties for leeward centerline heating theory.

C-4

ORIGINAL PAGE IS
OF POOR QUALITY

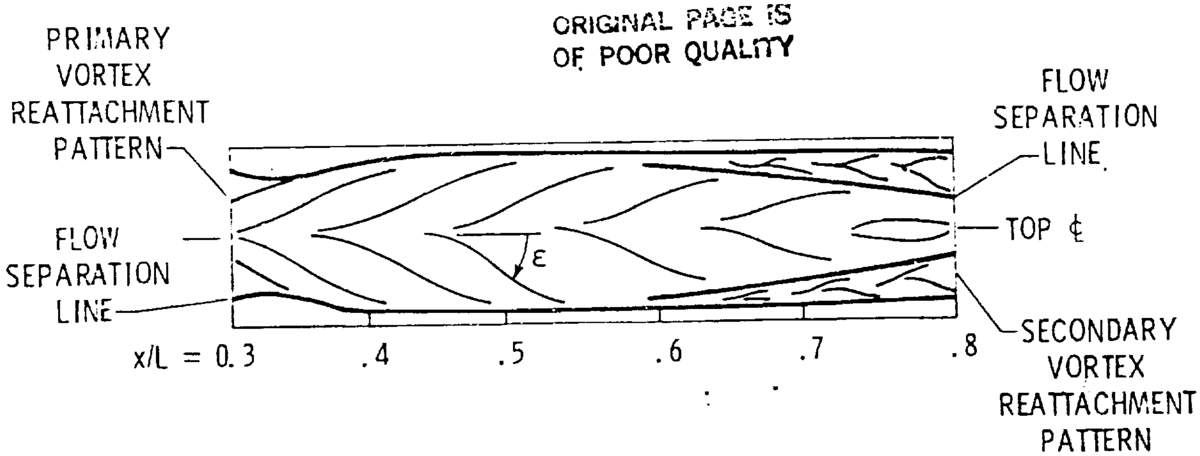

Figure 3.- Upper fuselage surface pattern showing measurement of flow angle.

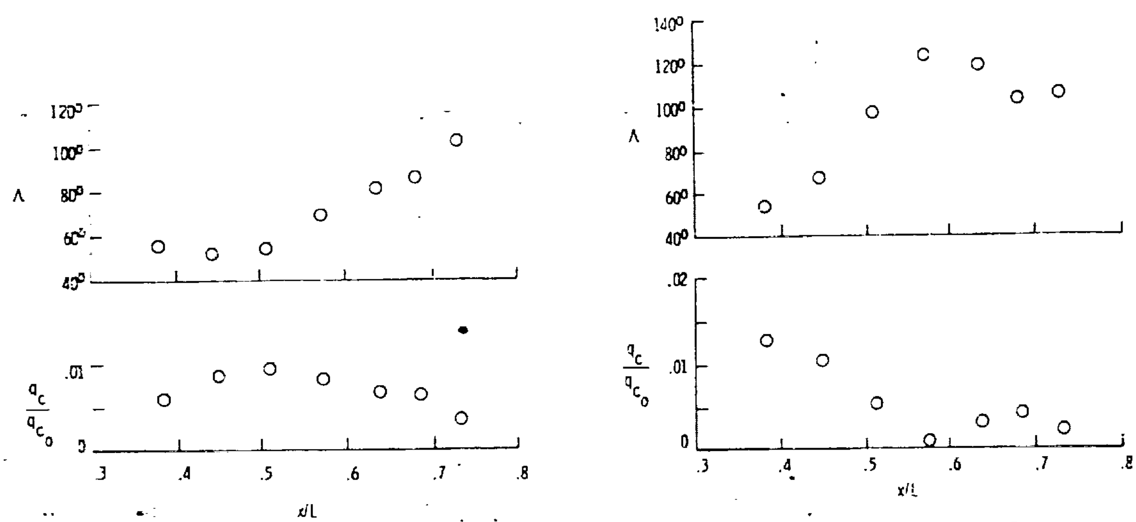

(a) $M_\infty = 10$; $\alpha = 20^\circ$; $Re_\infty = 2.37 \times 10^6$.

(b) $M_\infty = 6$; $\alpha = 30^\circ$; $Re_\infty = 5.4 \times 10^6$.

Figure 4.- Illustration of the inverse relation between effective sweep angle and leeward centerline heating rate.

ORIGINAL PAGE IS
OF POOR QUALITY

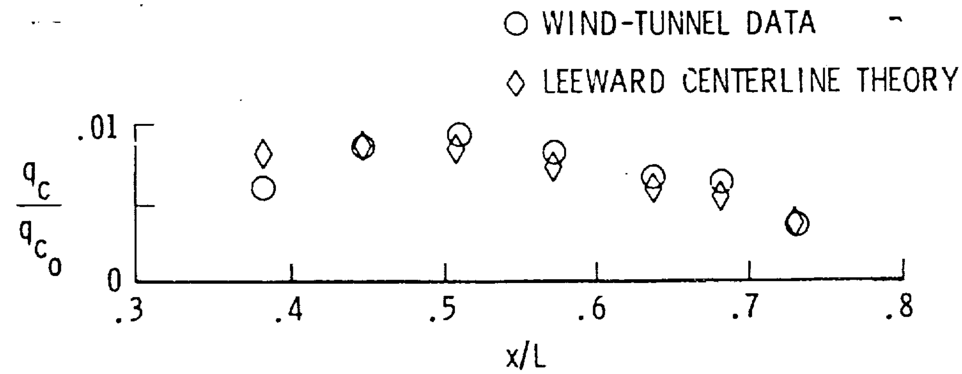

(a) $M_\infty = 10$; $\alpha = 20^\circ$; $Re_\infty = 2.37 \times 10^6$.

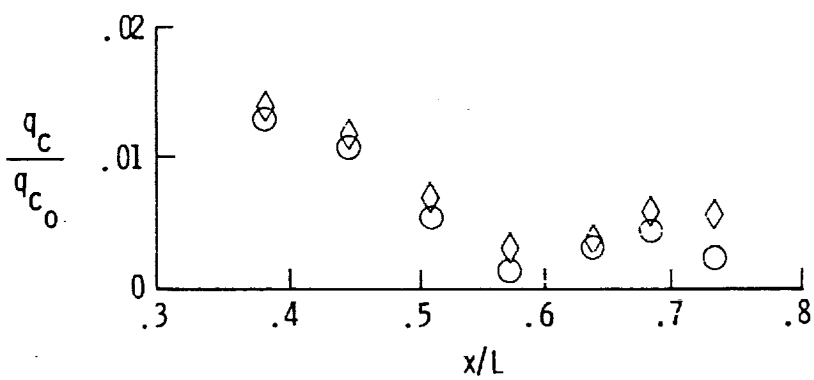

(b) $M_\infty = 6$; $\alpha = 30^\circ$; $Re_\infty = 5.4 \times 10^6$.

Figure 5.- Representative comparisons of leeward centerline heating predictions with wind tunnel data.

ORIGINAL PAGE IS
OF POOR QUALITY

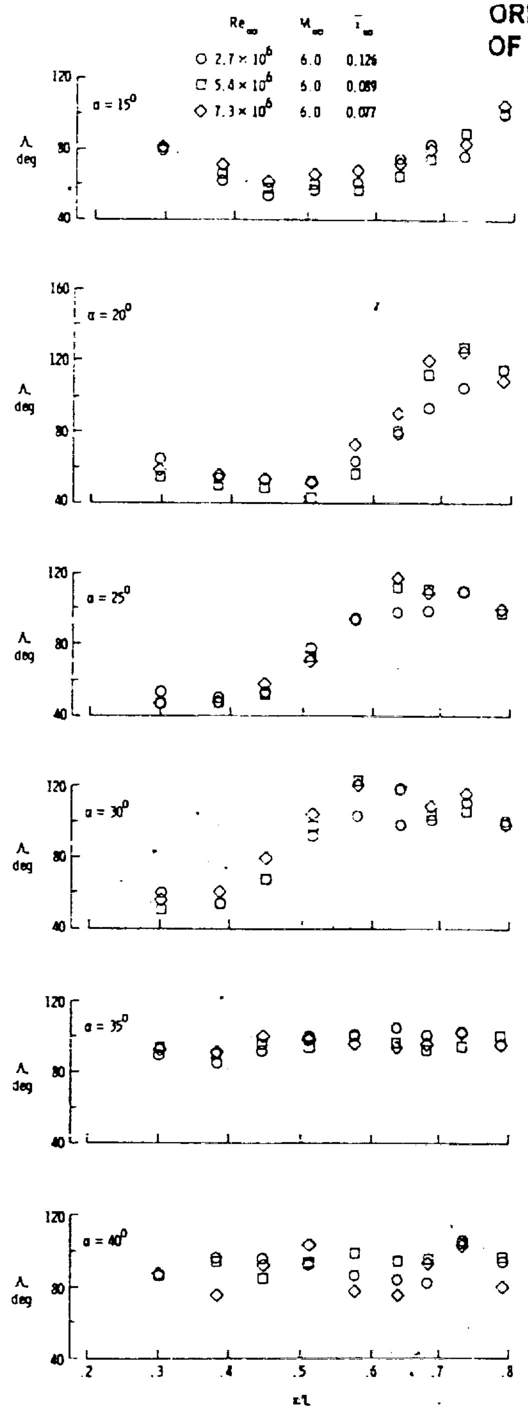

Figure 6.- Effective sweep angles measured from Mach 6 oil flow patterns.

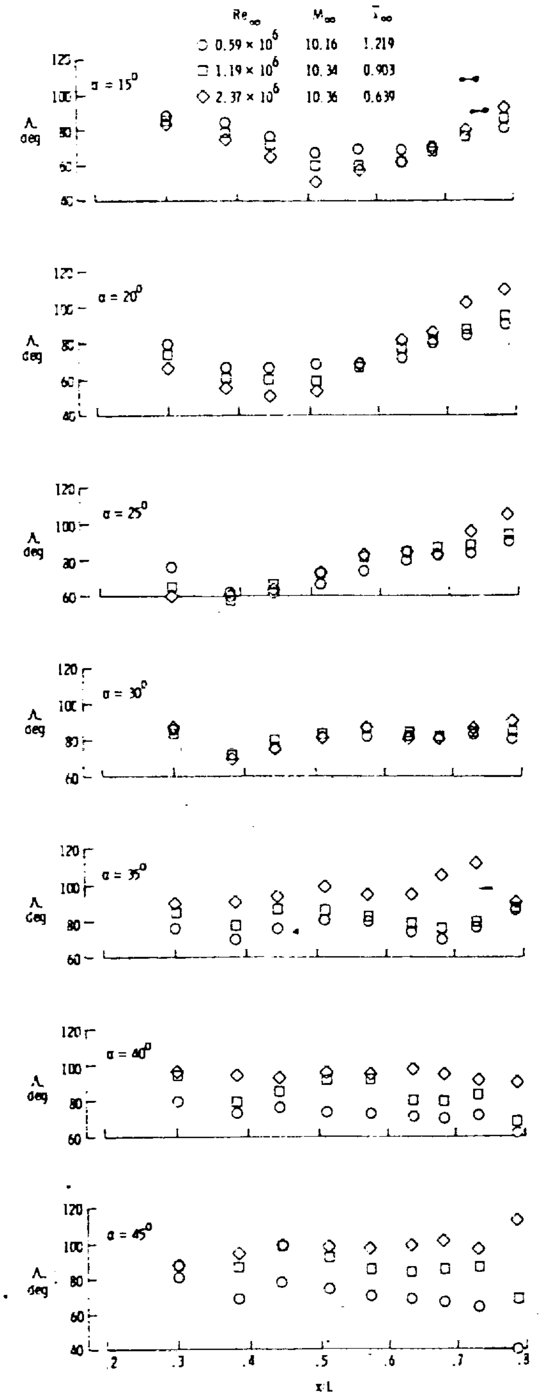

Figure 7.- Effective sweep angles measured from Mach 10 oil flow patterns.

ORIGINAL PAGE IS
OF POOR QUALITY

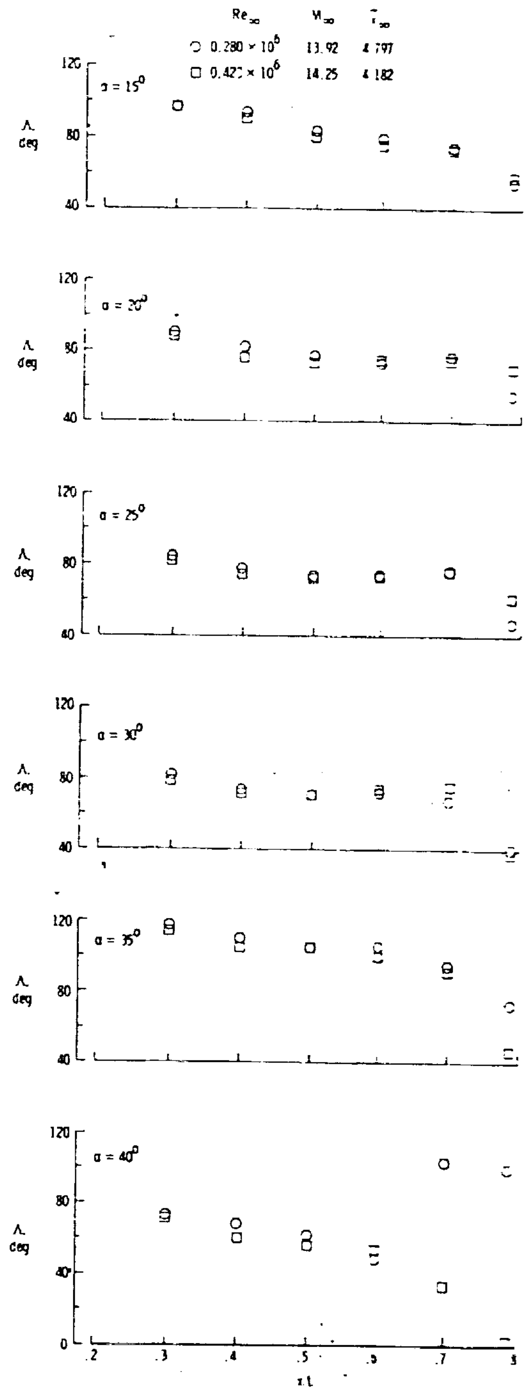

Figure 8.- Effective sweep angles measured from Mach 14 oil flow patterns.

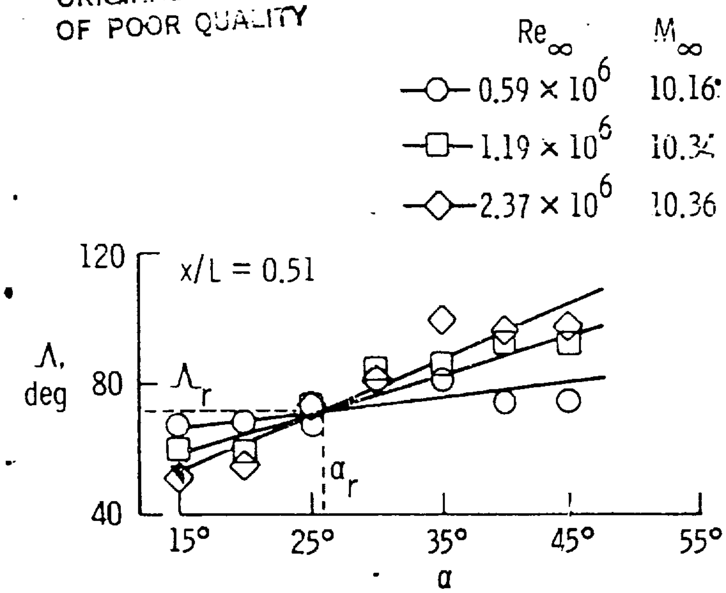

Figure 9.- Illustration of Reynolds number effect on Mach 10 wind tunnel sweep angles.

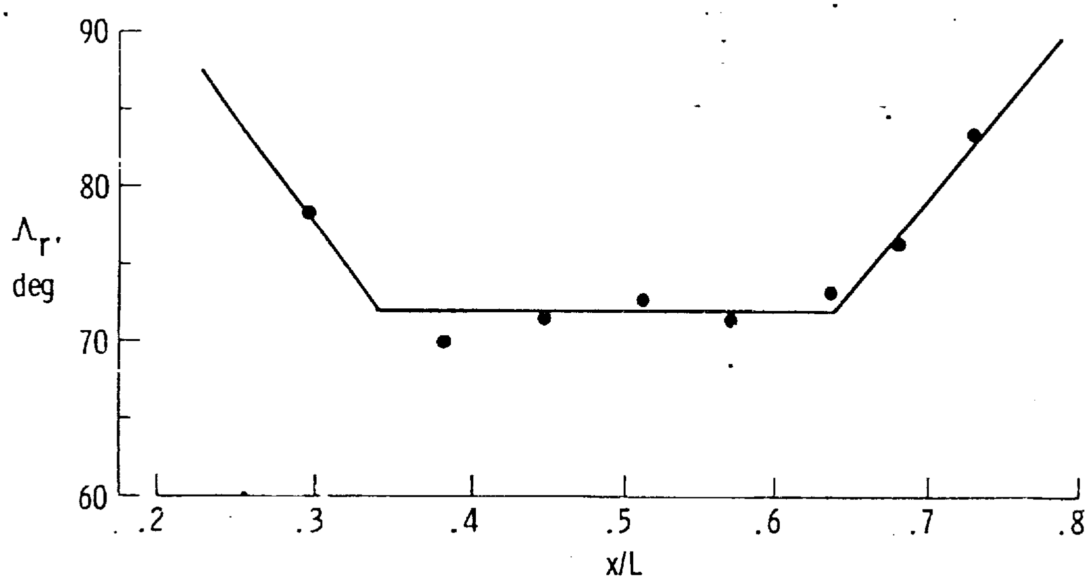

Figure 10.- Axial dependence of Λ_r.

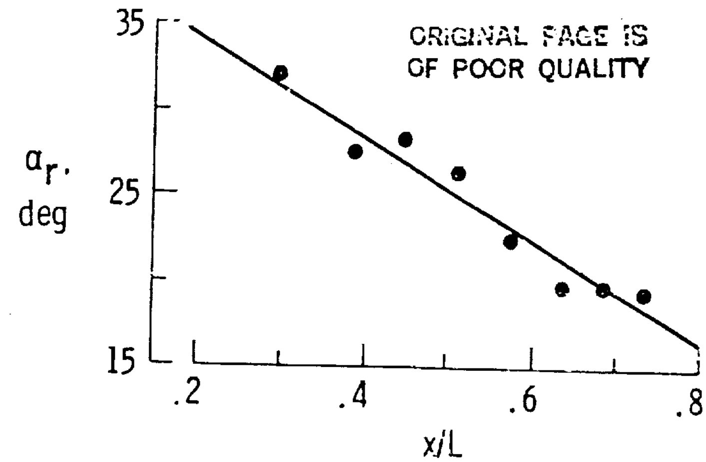

Figure 11.- Axial dependence of α_r.

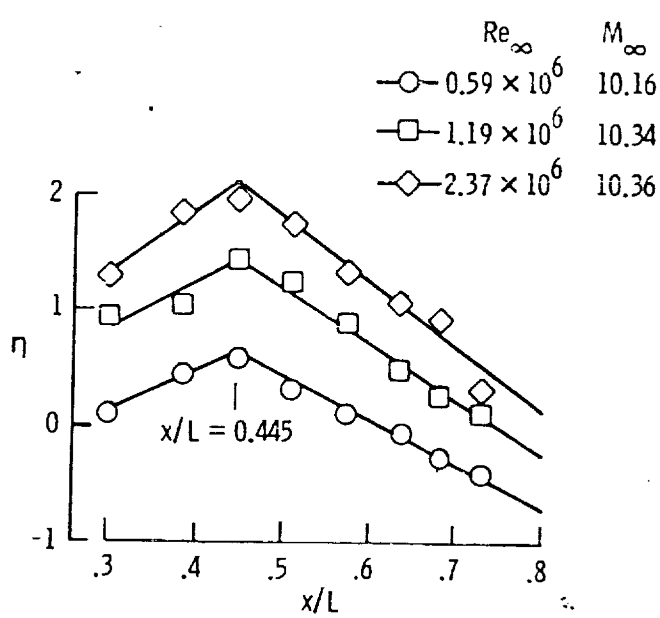

Figure 12.- Slope of Λ vs α as a function of Reynolds number and x/L.

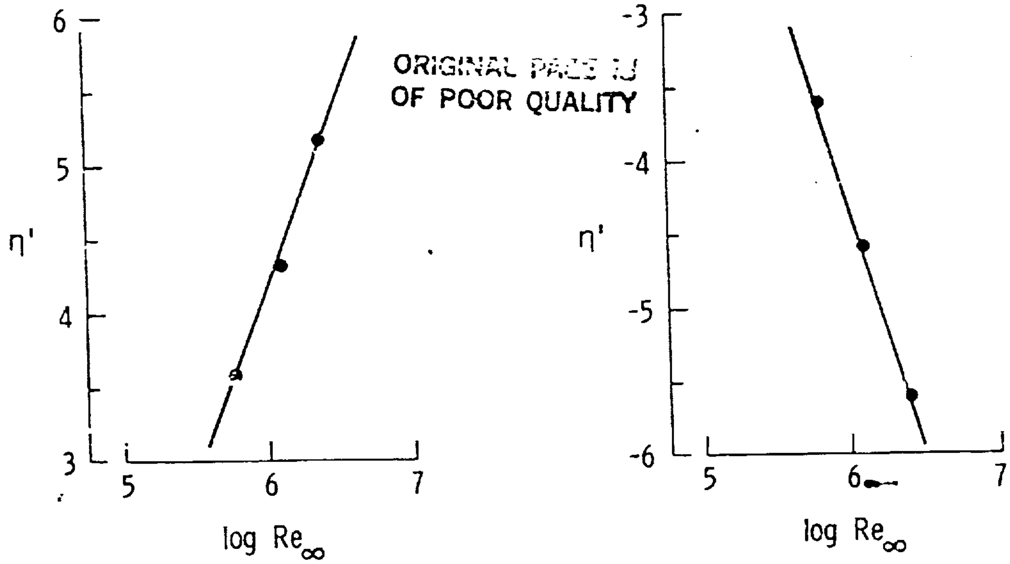

(a) $x/L < 0.445$.

(b) $x/L > 0.445$.

Figure 13.- Rate of change of η with respect to Reynolds number.

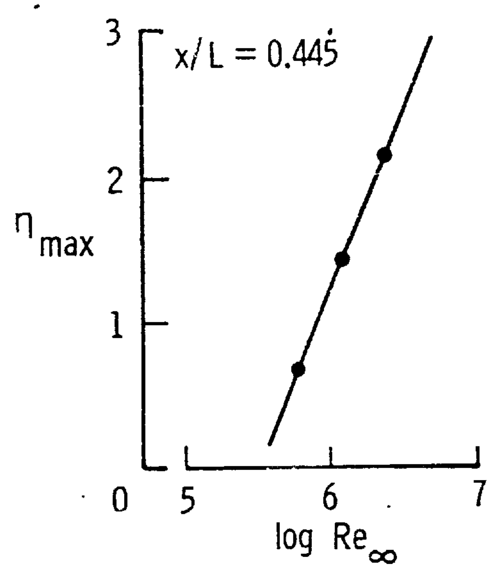

Figure 14.- Extrapolation of η at $x/L = 0.445$ in terms of Reynolds number.

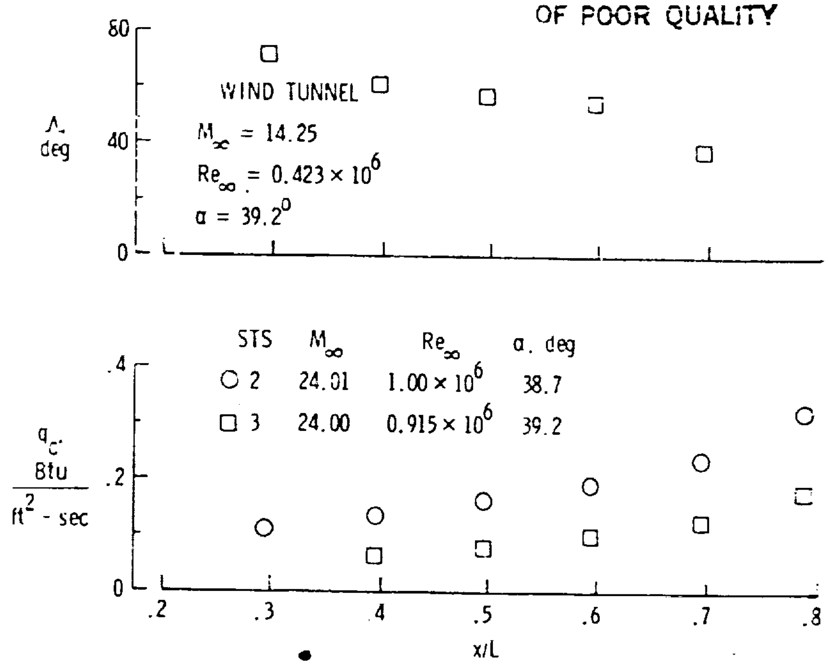

Figure 15.- Comparison of flight leeward centerline heating distributions near $M_\infty = 24$ with wind tunnel effective sweep angle variations.

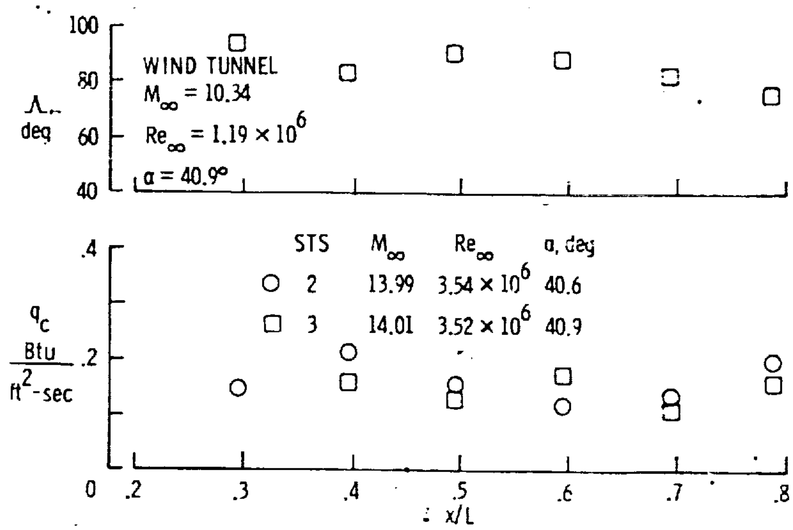

Figure 16.- Comparison of flight leeward centerline heating distributions near $M_\infty = 14$ with wind tunnel effective sweep angle variations.

ORIGINAL PAGE IS
OF POOR QUALITY

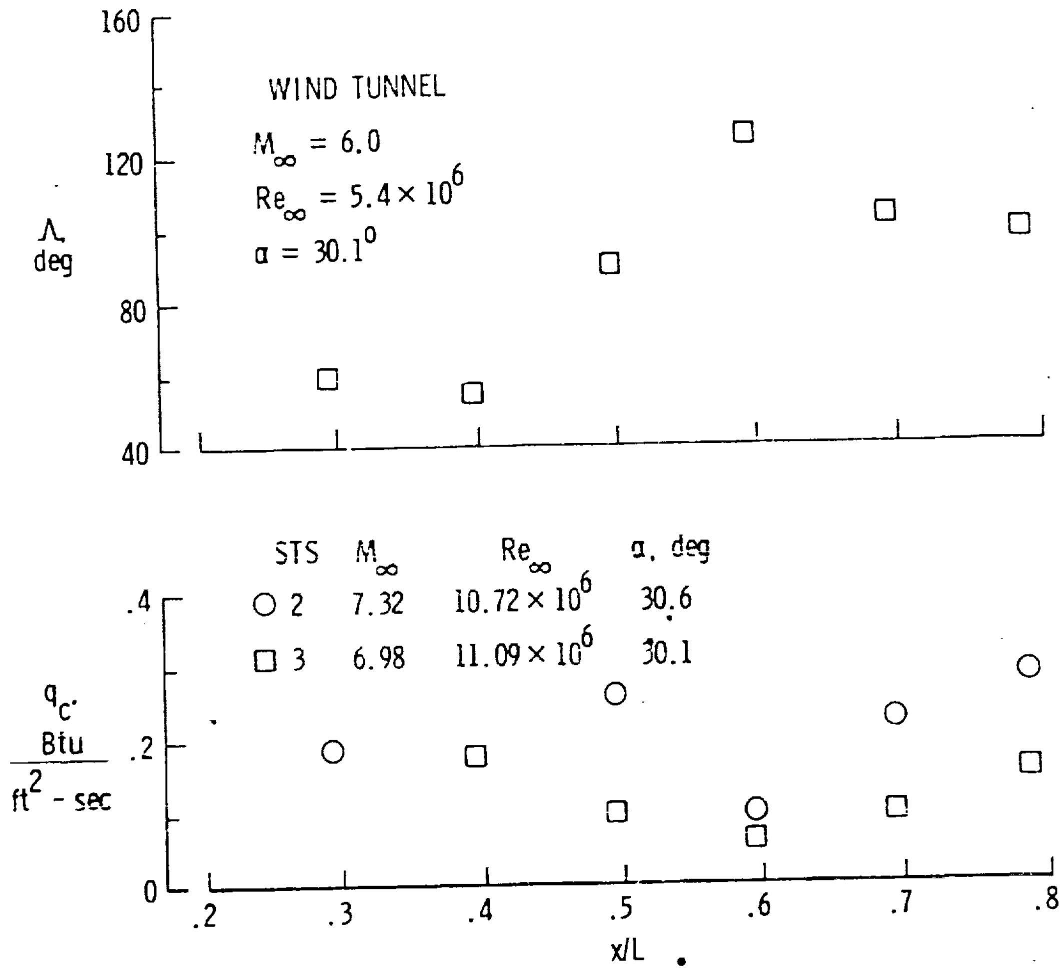

Figure 17.- Comparison of flight leeward centerline heating distributions near M_∞ = 7 with wind tunnel effective sweep angle variations.

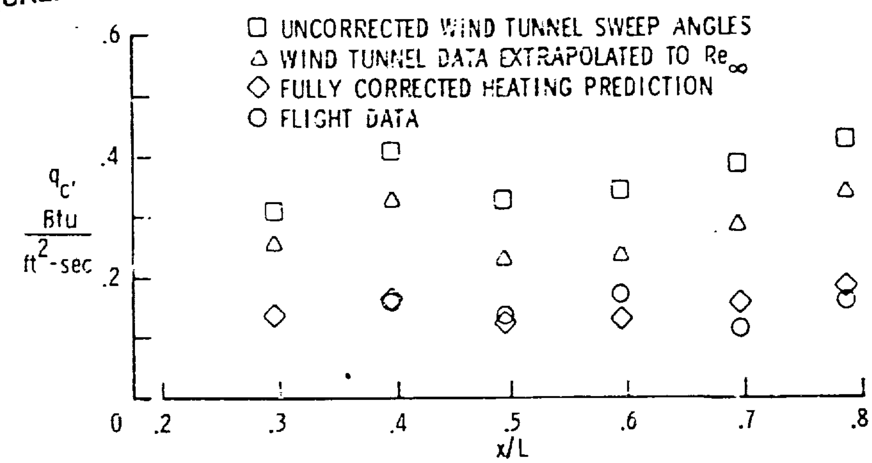

FLIGHT CONDITIONS: $M_\infty = 14.01$, $Re_\infty = 3.52 \times 10^6$, $\alpha = 40.9°$
TUNNEL CONDITIONS: $M_\infty = 10.34$, $Re_\infty = 1.19 \times 10^6$, $\alpha = 40.9°$

(a)

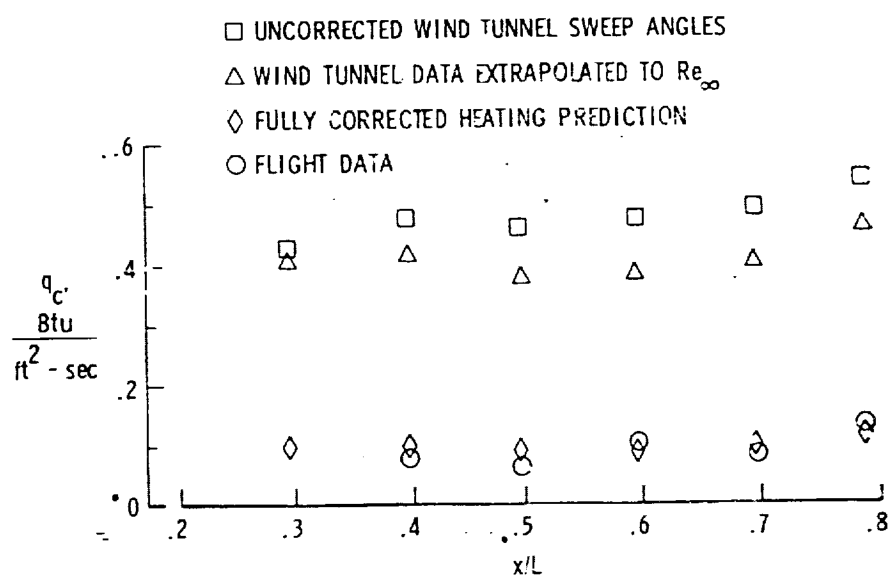

Flight conditions: $M_\infty = 20.00$, $Re_\infty = 1.53 \times 10^6$, $\alpha = 39.8^0$
Tunnel conditions: $M_\infty = 10.16$, $Re_\infty = 0.59 \times 10^6$, $\alpha = 39.8^0$

(b)

Figure 18.- Comparison of flight leeward centerline heating rates with predictions in various stages of correction for the effects of Mach number and Reynolds number.

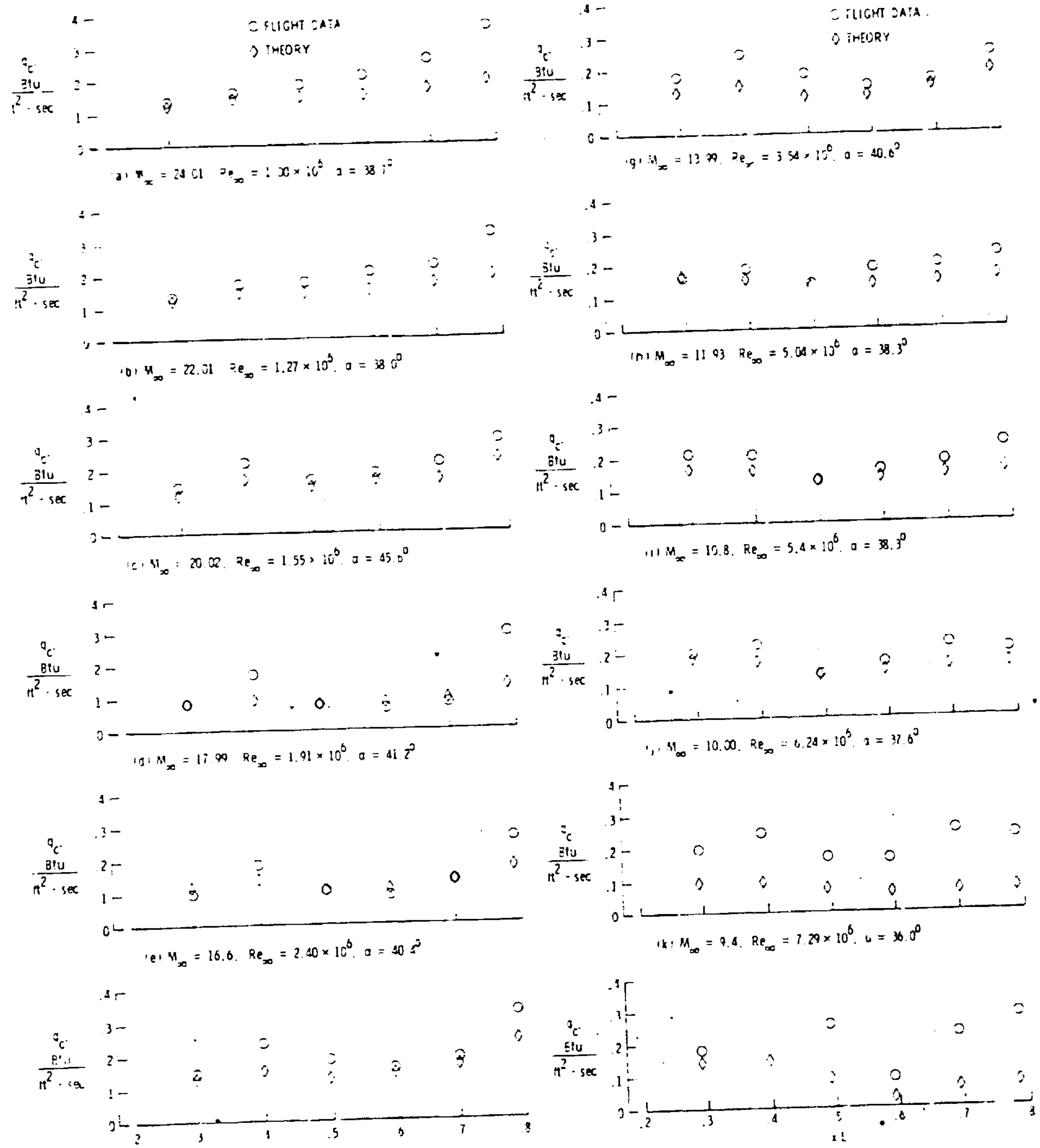

Figure 19.- Comparison of leeward centerline heating predictions with STS-2 flight data.

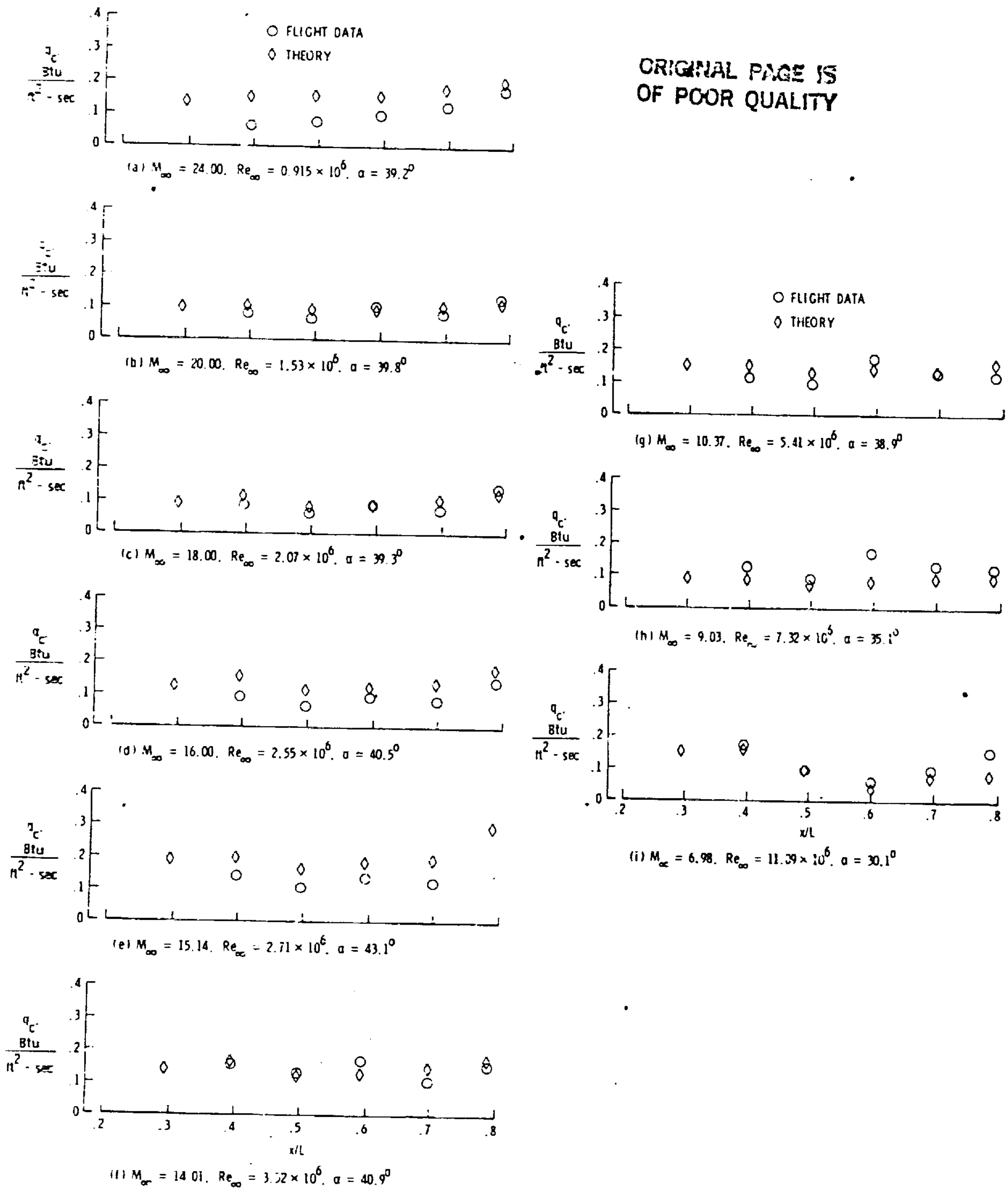

Figure 20.- Comparison of leeward centerline heating predictions with STS-3 flight data.

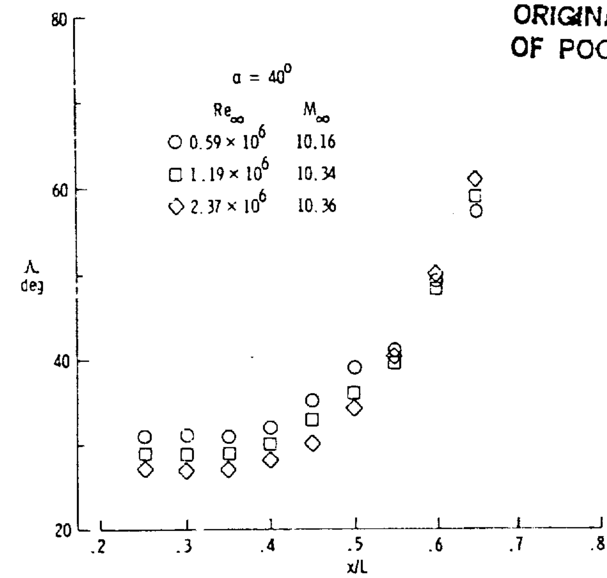

Figure 21.- Effective sweep angles resulting from side fuselage impingement.

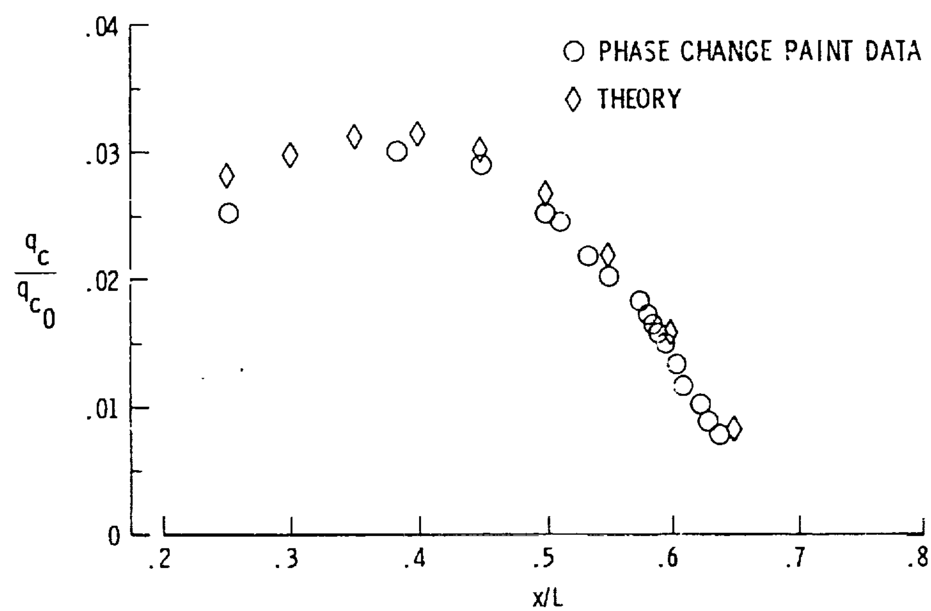

Figure 22.- Example of comparison between side fuselage impingement heating predictions and wind tunnel measurements for $M_\infty = 10.36$, $Re_\infty = 2.37 \times 10^6$ and $\alpha = 40^\circ$.

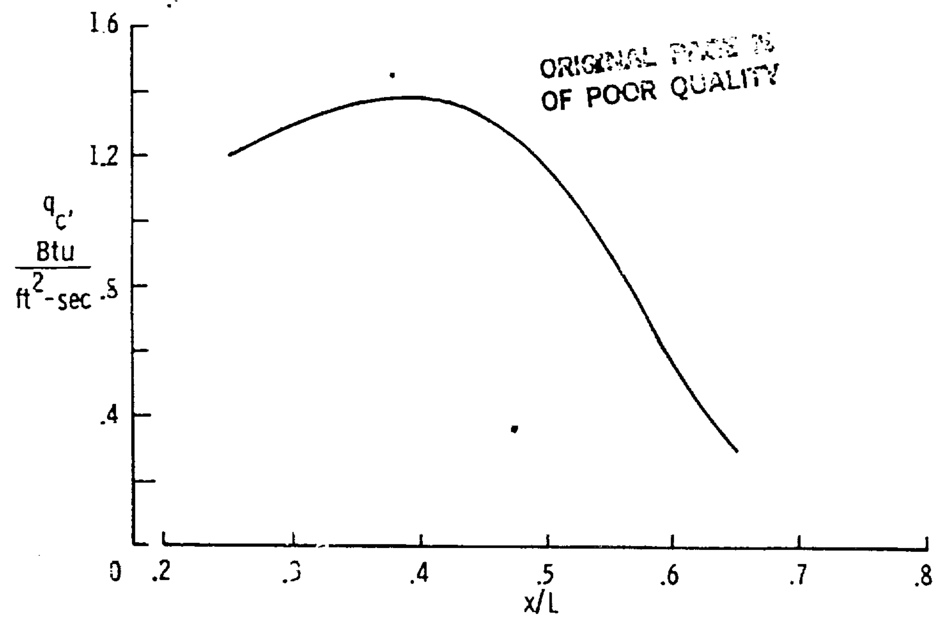

Figure 23.- Predicted side fuselage impingement heating for STS-3 at $M_\infty = 10.37$, $Re_\infty = 5.4 \times 10^6$, and $\alpha = 38.9^\circ$.

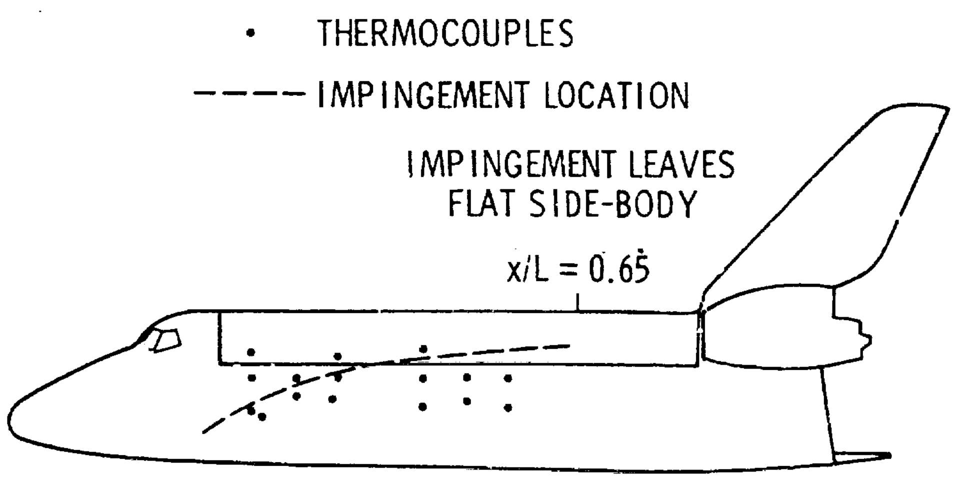

Figure 24.- Predicted location of impingement line with respect to side fuselage thermocouples at $M_\infty = 10.37$ and $\alpha = 38.9^\circ$ during STS-3.

ORIGINAL PAGE IS
OF POOR QUALITY

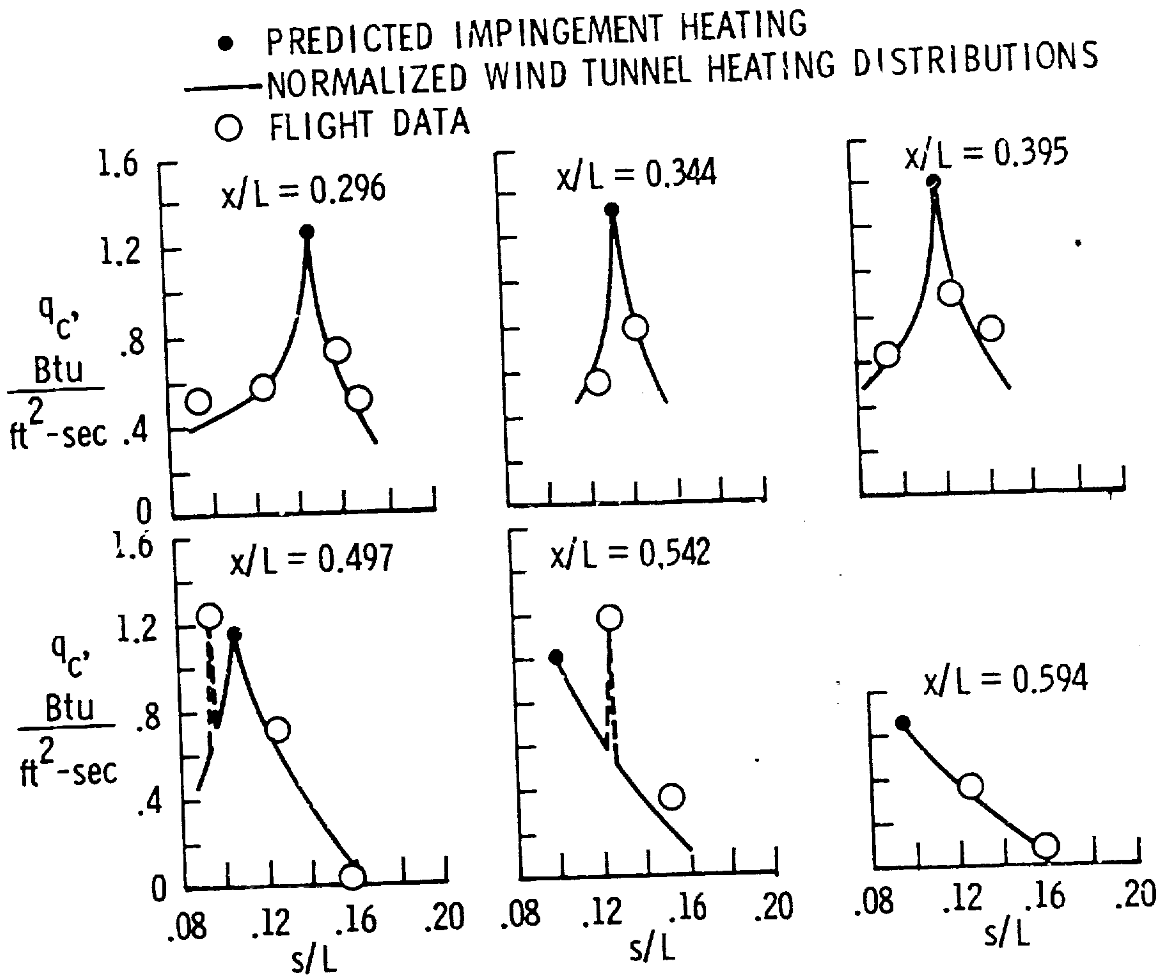

Figure 25.- Comparison of wind tunnel cross-sectional heating distributions and impingement heating predictions with STS-3 measurements at $M_\infty = 10.37$, $Re_\infty = 5.4 \times 10^6$, and $\alpha = 38.9^o$.

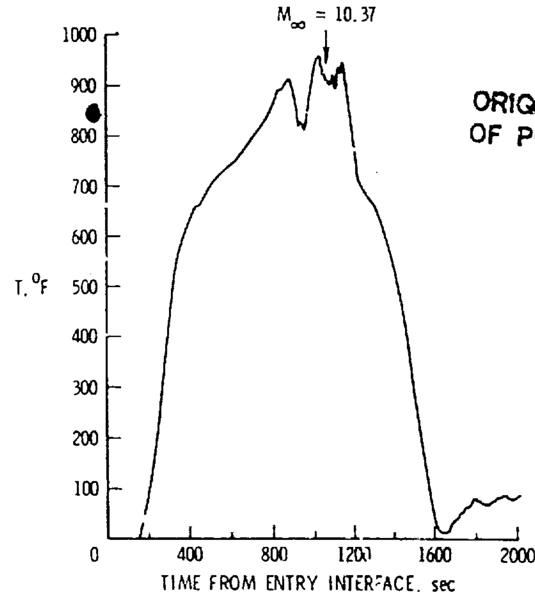

ORIGINAL PAGE IS
OF POOR QUALITY

(a) x/L = 0.497; s/L = 0.0950; V07T9924.

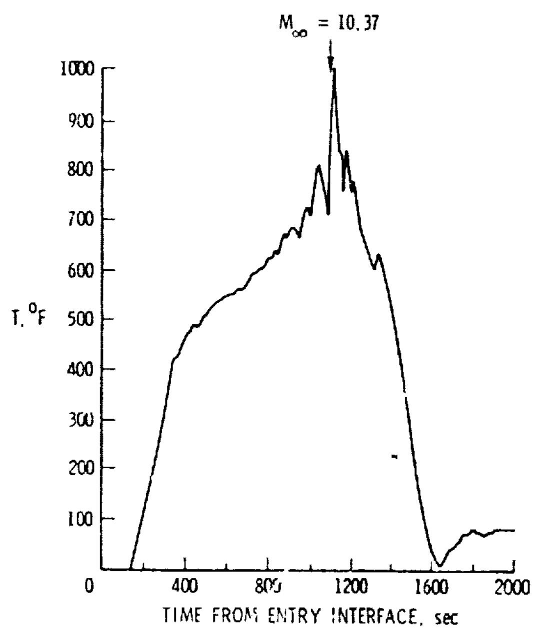

(b) x/L = 0.542; s/L = 0.1248; V07T9905.

Figure 26.- STS-3 side fuselage temperature time histories showing temperature fluctuations for entry times near M_∞ = 10.37.

ORIGINAL PAGE IS
OF POOR QUALITY

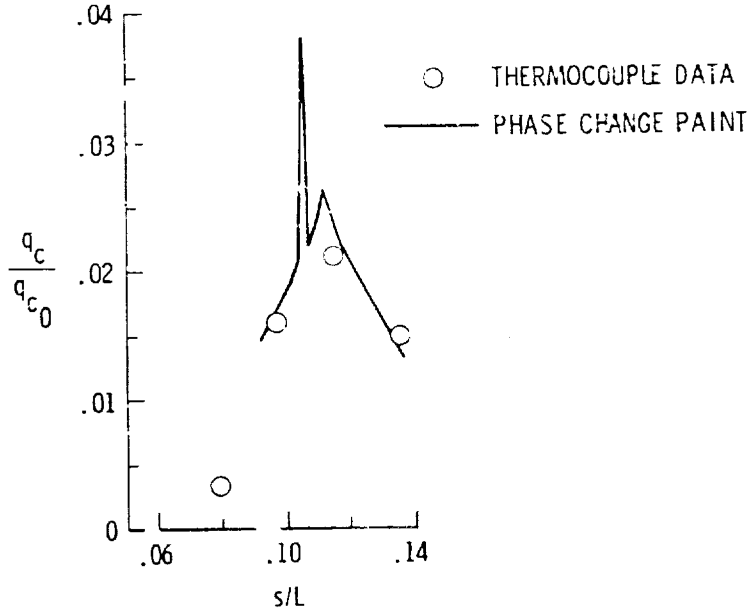

Figure 27.- Example of heating spike in wind tunnel data for $M_\infty = 6$, $Re_\infty = 5.4 \times 10^6$, and $\alpha = 40^\circ$ at $x/L = 0.447$.

Figure 28.- Pattern of "streak" heating in phase change paint test at $M_\infty = 6$, $Re_\infty = 5.4 \times 10^6$, and $\alpha = 40^\circ$.